Monthly Notices of the ROYAL ASTRONOMICAL SOCIETY

MNRAS **529,** 1207–1221 (2024) https://doi.org/10.1093/mnras/stae603
Advance Access publication 2024 February 27

Iron depletion in mineral dust grains from Saturn's main rings

Simon Linti [1]★ Frank Postberg,[1]★ Hsiang-Wen Hsu,[2] Jon K. Hillier,[1] Christian Fischer,[3] Mario Trieloff,[3] Jürgen Schmidt,[1] Sascha Kempf[2,4] and Ralf Srama [5]

[1]*Institut für Geologische Wissenschaften, Freie Universität Berlin, D-12249 Berlin, Germany*
[2]*Laboratory for Atmospheric and Space Physics, University of Colorado, Boulder, CO 80303, USA*
[3]*Institut für Geowissenschaften, Universität Heidelberg, D-69120 Heidelberg, Germany*
[4]*Department of Physics, University of Colorado, Boulder, CO 80309, USA*
[5]*Institut für Raumfahrtsysteme, Universität Stuttgart, D-70569 Stuttgart, Germany*

Accepted 2024 February 26. Received 2024 February 26; in original form 2023 November 14

ABSTRACT

During the Grand Finale orbits, Cassini's Cosmic Dust Analyzer (CDA) recorded *in situ* mass spectra of ice and mineral nanodust grains ejected from Saturn's main rings falling into the planet's atmosphere. We present a compositional analysis of the mineral dust fraction employing a spectral deconvolution method to determine the elemental composition of these grains. The results indicate a relatively homogenous composition of exclusively Mg-rich silicates, with Mg, Si, and Ca close to CI chondritic abundances but a significant depletion in Fe and only traces of organic material at best. The Fe depletion becomes even more pronounced when compared to Fe-rich interplanetary dust particles encountered by CDA in the Saturnian system, which are assumed to contaminate and darken the main rings over time. We discuss potential explanations for the depletion, from which we favour compositional alteration of the infalling dust grains by impact-triggered chemistry in combination with dynamical selection effects and instrumental bias as the most plausible ones. This might cause an accumulation of Fe in the main rings over time, most likely in the form of oxides.

Key words: methods: data analysis – planets and satellites: individual: Saturn – planets and satellites: rings.

1 INTRODUCTION

The investigation of Saturn's rings has fascinated scientists since their discovery. Observations with various techniques over the last decades revealed structural details and the composition of the rings (Pollack 1975; de Pater & Dickel 1991; Spilker et al. 2003; Dougherty, Esposito & Krimigis 2009). The best insight into the ring dynamics and composition was delivered by the Cassini-Huygens mission, which explored Saturn's ring system over 13 yr. Most compositional analyses were made with remote sensing techniques, showing that Saturn's main rings consist mostly of water ice, with the non-icy components, making up only a few per cent of the rings' mass, in agreement with silicates (Morris et al. 1985; Cruikshank, Imanaka & Dalle Ore 2005; Clark et al. 2008), but also organic compounds (e.g. Cuzzi & Estrada 1998; Nicholson et al. 2008; Bradley et al. in review), as well as amorphous carbon (Cuzzi & Estrada 1998; Cuzzi et al. 2018) and maybe fine-grained iron and/or hematite (Clark et al. 2012). Regarding silicates, the most recent remote sensing results infer volume silicate fractions varying between 0.1 and 0.5 per cent for the A and B rings (Zhang et al. 2017a), whereas the C ring was found to contain the highest silicate abundance – 1–2 per cent in most areas and a maximum of 6–11 per cent in the centre of the ring (Zhang et al. 2017b). Regarding the non-icy ring material, Cuzzi et al. (2018) consider these values as upper limits for silicates.

In this study, we focus on the ring particles detected during the Cassini Grand Finale orbits from 2017 April to September. During this period, the Cassini spacecraft traversed 22 times through the gap between the inner edge of the D ring and Saturn's cloud tops, providing unprecedented opportunities to study Saturn's main rings with *in situ* instruments. The measurements were carried out by the Cosmic Dust Analyzer (CDA), an impact ionization time-of-flight mass spectrometer capable of providing elemental compositional information of individual grains impacting the instrument target at speeds of at least several kilometres per second (Srama et al. 2004). CDA observations during the Grand Finale mission were motivated by an earlier study showing that charged dust particles could be dynamically unstable and propagate along magnetic field lines connecting Saturn and its rings (Northrop & Hill 1982). Because of the northward offset of Saturn's dipolar magnetic field, charged dust particles with sizes of 10 s of nm are expected to fall preferably into Saturn's Southern hemisphere (Northrop & Hill 1982; Ip 1983; Connerney 1986). Initial results published by Hsu et al. (2018) show that (i) nanodust 10 s of nm in size forms the dominant population in between Saturn and its rings, while grains larger than ∼0.1 μm have a spatial density orders of magnitude lower; (ii) the measured particle flux exhibits a significant north–south asymmetry, consistent with the pre-Cassini dynamical analysis, suggesting the detected particles, likely released as impact ejecta, indeed originated from the

★ E-mail: s.linti@fu-berlin.de (SL); frank.postberg@fu-berlin.de (FP)

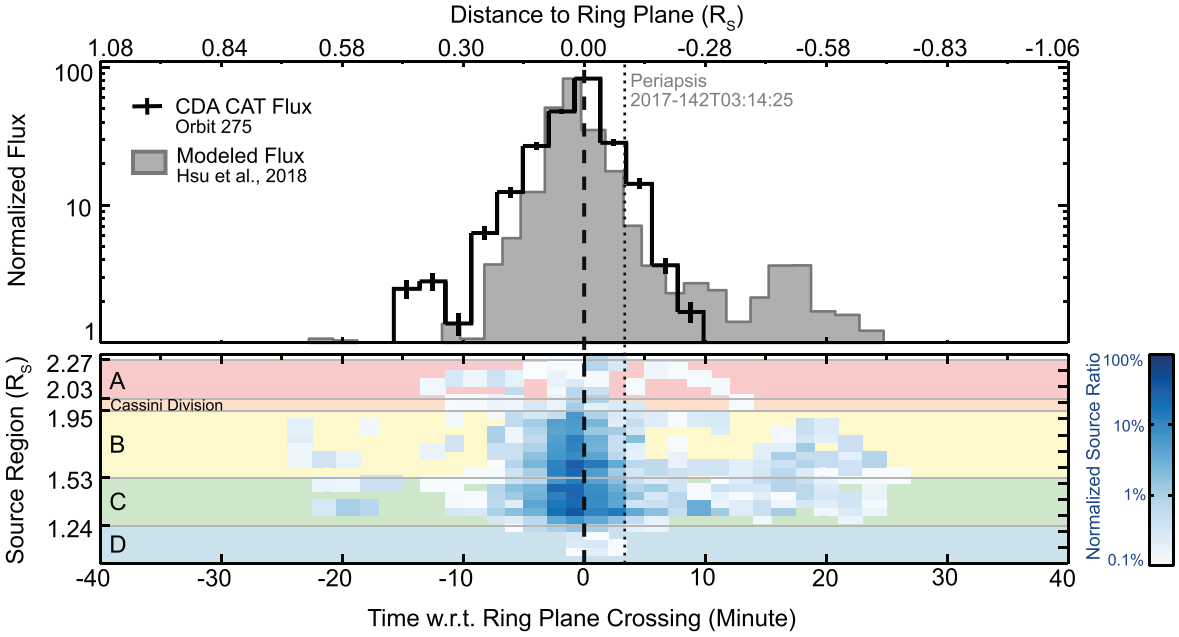

Figure 1. Nanodust flux profile registered by the Chemical Analyzer Target (CAT) of Cassini's CDA during orbit 275. The upper panel shows the measured and modelled flux profiles as the spacecraft moved southwards crossing the ring plane. In the model, the grain radius is set to be 20 nm and the bulk density is 1 g cm^{-3}. Material-specific densities, i.e. for non-icy particles, were not considered here (dynamical models assuming densities of 3 g cm^{-3} for mineral grain are presented in Section 3). The lower panel shows the modelled source region distribution for particles detected at locations with respect to the ring plane. The results suggest most originated from the B and C rings (adapted from Hsu et al. 2018).

main rings; and (iii) water ice and silicate grains are identified as the main compositional classes of the detected nanodust particles, with silicates accounting for about 30 per cent of those spectra to which a composition type could be assigned. The only other non-water constituents detected are small amounts of unspecified organic material in a few ice grains.

Fig. 1 shows the dynamical model established using CDA measurements (Hsu et al. 2018), indicating most grains detected by CDA originated from the B and C rings. This suggests that silicate particles detected by CDA should be highly representative of the non-icy constituent in Saturn's main rings.

The work presented here represents a detailed investigation of this ring debris, focusing on the silicate fraction. The main ring particles are all high-speed detections, with an average impact speed of around 30 km s^{-1}. This high impact speed produces mass spectral features almost exclusively from elemental cations (see Section 2). The high impact speed on to the instrument target allowed the detection of particles only 10 s of nm in size.

Table 1. List of the Grand Finale orbits used for the analysis. Given are the UTC of the respective ring plane crossings (RPX), the number of identified silicate particles, and the articulation of CDA during the respective RPX.

Rev	UTC of RPX	Number of silicate spectra	CDA articulation (°)
273	2017–129T06:13:21	13	105
275	2017–142T03:11:05	33	74
278	2017–161T12:41:20	9	47
279	2017–167T23:52:04	39	96
280	2017–174T10:53:45	13	45
281	2017–180T22:10:33	31	155
283	2017–193T20:43:37	35	127
284	2017–200T07:50:09	9	270
287	2017–219T17:18:35	52	123
288	2017–226T04:18:28	18	105
290	2017–239T02:15:21	14	115
291	2017–245T13:12:00	34	125
292	2017–252T00:10:04	21	106

2 MATERIALS AND METHODS

2.1 The data set

For the analysis, data of 13 Grand Finale orbits were used (Table 1). Although the pointing was not optimized for CDA during each of the 13 ring plane crossings (RPXs), the largest number of spectra were recorded within ±20 min from the RPXs, which represents the time frame where modelling predicts that most particles stem from the main rings (Fig. 1; Hsu et al. 2018). The data set was restricted to those spectra recorded by CDA with signals strong enough to attempt spectral classification. From a total of 1353 spectra, 362 spectra of possible silicate particles were identified (∼27 per cent, Table S1), divided into four qualitative groups (Table 2). The remaining fraction is dominated by water ice spectra (∼57 per cent) and currently unclassified spectra (∼16 per cent) with ambiguous spectral signatures. The 41 spectra of the lowest confidence level ('silicate uncertain') were not used for the compositional analysis in this work.

The silicate spectra were first calibrated onto a mass scale, using the CDA data analysing software. If present, the mass lines of Fe^+ (main isotope 56 u) and Rh^+ (103 u) were used to calibrate the spectrum. For spectra without a significant Fe^+ mass line, Mg^+ (main isotope 24 u) could be used instead, although with a higher uncertainty. This is because Na^+ (23 u) is often not resolved from the neighbouring Mg^+ peak and thus might also contribute to the peak maximum. Spectral calibration from a time to a mass domain follows the relation $t = a\sqrt{m} + b$, for ions of mass m arriving at

Table 2. Spectral criteria of the four identified silicate groups. The percentages reflect the fractions of the full data set. σ is the standard deviation of the local spectrum noise.

Spectral type	Spectral criteria
Silicate sure[a] (117 spectra, 8.6 per cent)	■ High S/N
	■ Merged Na^+ and Mg^+ lines $\geq 4\,\sigma$
	■ Merged Al^+ and Si^+ lines $\geq 2\sigma$
	■ C^+ line $\geq 3\sigma$
Silicate likely[b] (33 spectra, 2.4 per cent)	■ Generally high S/N
	■ Merged Na^+ and Mg^+ lines mostly $\geq 4\sigma$
	■ Merged Al^+ and Si^+ lines mostly $\geq 2\sigma$
	■ Slightly ambiguous due to absence of some mineral-forming ions, mostly Ca^+ or Fe^+
Silicate weak[c] (171 spectra, 12.6 per cent)	■ Slightly ambiguous due to low S/N
	■ Merged Na^+ and Mg^+ lines $< 4\sigma$
	■ Merged Al^+ and Si^+ lines $< 2\sigma$
Silicate uncertain (41 spectra, 3.0 per cent)	■ Highly ambiguous due to low S/N
	■ Absence of important mineral-forming ions, such as Si^+ and Fe^+
	■ Overall spectral shape still agrees better with silicates than ice

[a]Used for individual compositional analysis in Figs 4–7.
[b,c]Used for statistical purposes only in Figs 3, 4, 5, 7, and 8.

time t. Here, the stretch parameter a is related to the geometry of CDA and the applied field strengths (e.g. Hillier et al. 2006), and the shift parameter b is related to instrument triggering. During the last two Grand Finale orbits, the potential at the instrument target was increased from about 1000 to 1400 V, shortening the TOF of the ions, resulting in smaller values of a and more compressed spectra with slightly decreased mass resolution. These spectra are excluded from the co-added spectra (see below).

Table 2 also summarizes the spectral features used as criteria to classify the four silicate groups. The qualitative criteria of 'silicate sure' spectra were considered as sufficient for quantitative analysis and their compositions are analysed individually. Assignment as silicates for the spectra of the second and third group ('likely' and 'weak') is slightly ambiguous, and therefore they are not used for individual compositional analysis. Since the 'weak' spectra, however, account for more than 50 per cent of the silicate data set, they are investigated co-added in a single sum spectrum that provides sufficient signal-to-noise ratios (S/Ns) for quantitative analysis. In later discussion, they are referred to as 'weak signal'. The fourth group ('silicate uncertain') comprises highly ambiguous spectra; however, their spectral appearance might still agree best with silicates. They are not considered in the compositional analysis.

2.2 Spectral classification

The spectra identified as silicate show mass lines of Si^+ and other mineral-forming ions, such as Mg^+, Ca^+, and Fe^+ (Fig. 2a), although, except for Si^+, not necessarily all of them are identifiable in any single spectrum. In most cases, together with Si^+, the lines of Mg^+, Fe^+, and Al^+ were sufficient to determine the siliceous nature of the grain. Three silicate spectra show an additional peak attributed to S^+ (Fig. 2b), which points at an additional sulphur-bearing phase in these grains that could possibly be entrained into these particles by a secondary effect (see Section 4, Scenario 3b).

In addition to the particle ions, potential contaminants such as ions of Na^+, K^+, and C^+ are observable in the spectra. Rh^+ is the target material, which is excavated and ionized by particles impacting at speeds higher than approximately 8 km s^{-1} (Postberg et al. 2009a), and therefore is frequently seen in the analysed spectra. The mass lines of Na^+ and K^+ are, at least to a greater part, related to an instrument target contamination, although they could theoretically be particle constituents. After multiple plume encounters during the close Enceladus flybys between 2008 and 2015, the CDA Chemical Analyzer Target (CAT) was increasingly contaminated with residues deposited, or recondensing, on to the target from salt-rich ice grains (Postberg et al. 2009b, 2011). Varying amounts of the contamination layer were ionized by every impacting particle studied in this work, leading to potentially significant contamination peaks, predominantly Na^+, with varying amplitudes in CDA's cation mass spectra.

Oxygen is visible in most of the spectra in the data set (Table 2). It generally appears in spectra recorded from grains impacting at about 20 km s^{-1} or more and can be used as a speed indicator (Postberg et al. 2009a; Fiege et al. 2014). Oxygen cannot be ruled out as a potential minor contaminant, stemming from the instrument target (Postberg et al. 2009a), but to a greater part is likely to stem from the silicate particles (Hillier et al. 2012; Fiege et al. 2014; Hsu et al. 2018).

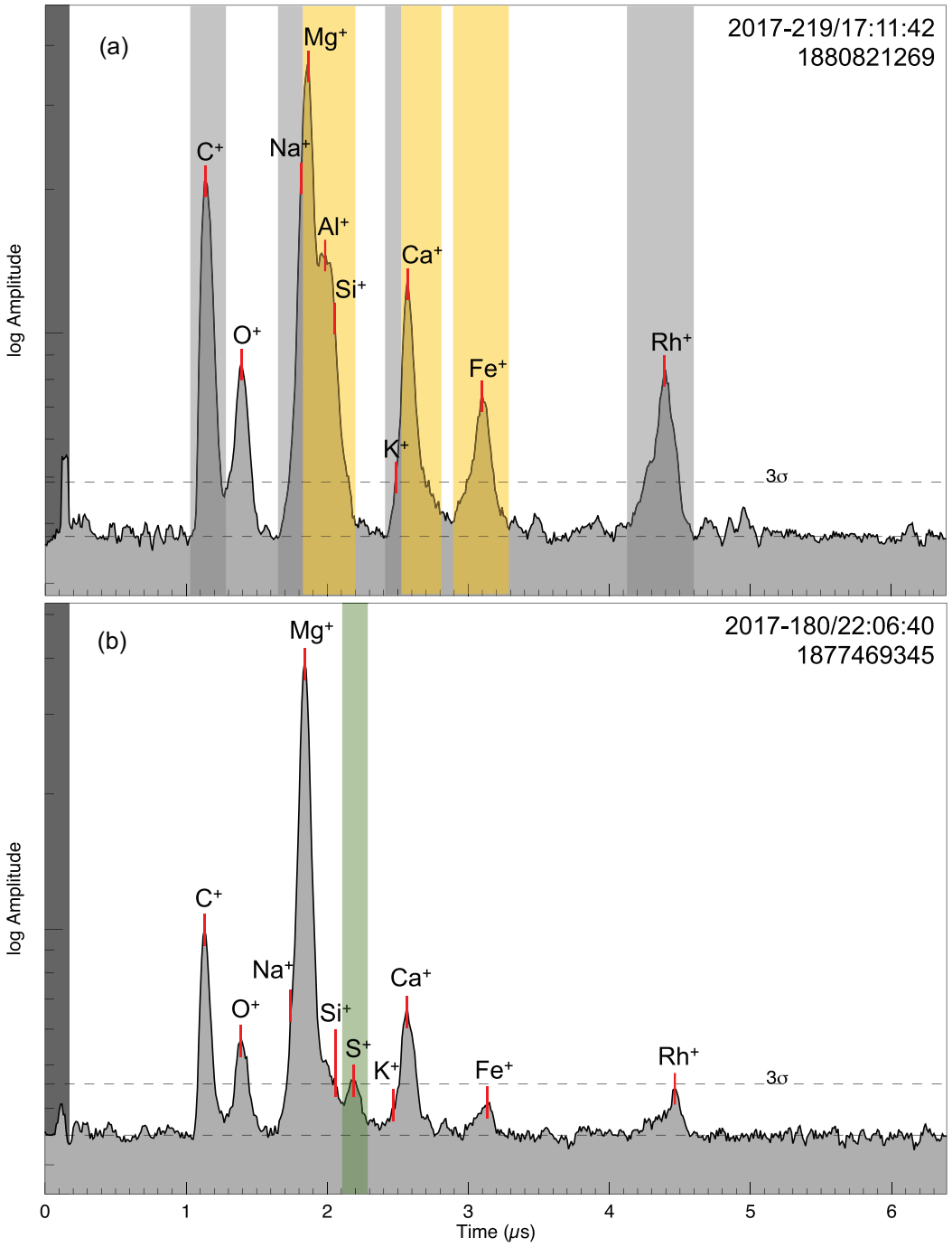

Figure 2. (a) An example of a typical high S/N silicate spectrum detected during the Grand Finale orbits. Particle constituents are highlighted in yellow, contaminants and target material are highlighted in grey. The O^+ mass line is most likely to be from a particle constituent, but contributions from target contamination cannot be ruled out. (b) Silicate spectrum with a rare but significant sulphur peak, highlighted in green. The upper dashed line represents the significance level (3σ) above the average spectrum noise (lower dashed line).

2.3 Particle size calculation

The radii of the silicate particles are estimated to range from about 20 to 100 nm, with 81 per cent being between 20 and 40 nm and 19 per cent being larger (Fig. 3). The particle radii are determined from the calculated masses, assuming a spherical particle shape and an average density of 3 g cm^{-3}. The formula that was used to calculate the particle masses was constructed empirically from CDA dust accelerator experiments with iron particles (Srama et al. 2004) and is

$$m = 48.2 \times \left(\frac{QI}{v^5}\right)^{0.91} \quad (1)$$

with the impact speed v in km s^{-1}, assumed to be similar to the spacecraft speed during the ring plane crossings, typically around 30 km s^{-1}; ion yield QI in C; and mass m in kg.

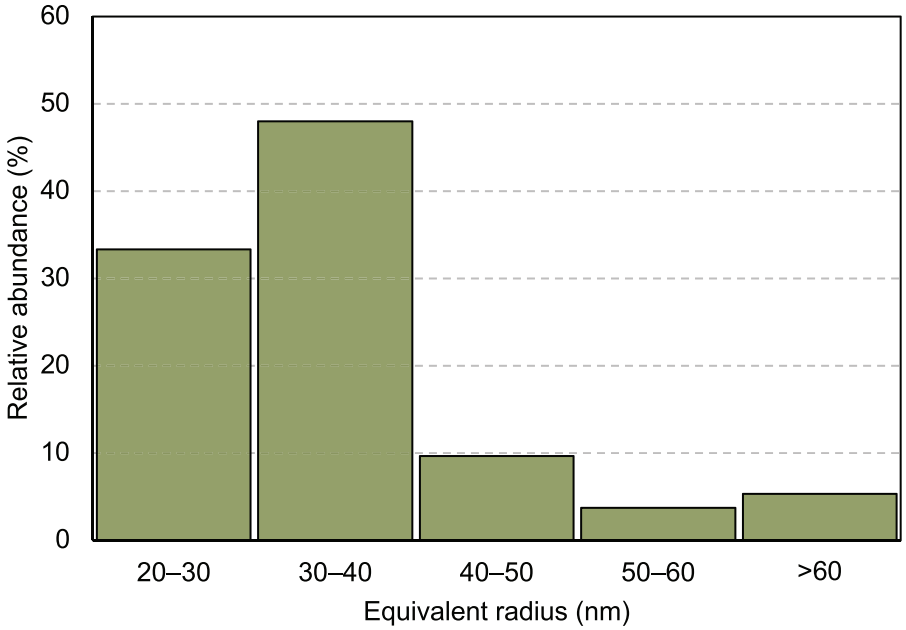

Figure 3. Size distribution of silicate particles, showing a maximum of 48 per cent between 30 and 40 nm. The decrease below 30 nm does not reflect the actual abundances, but CDA's detection limit, below which we do not receive reliable spectral signals of all particles of this size. Note, that there are no silicate particles with calculated equivalent radii above 120 nm detected in any of Cassini's ring plane crossings in the Grand Finale orbits, although the detector was sensitive to maximum radii of about 350 nm. Please note that the absolute size determination using the CDA's QI signal is affected by significant uncertainties (see the main text).

The mass and size estimates, based on the QI signal, are affected by significant uncertainties for individual grains. This is mostly caused by the remaining uncertainty of the exact impact speed and the fact that the calibration of CDA used iron dust particles and the ion yield of the silicates investigated here might be different. This amounts to an uncertainty of a factor of 2 for the absolute sizes given here (Hsu et al. 2018). However, the given sizes are more reliable for a larger ensemble, specifically when only relative sizes are considered (i.e. particles in bin A are twice as large as in bin B).

2.4 Deconvolution

The resolving power of CDA, from its mass resolution of $m/\Delta m$ = 20–50 (Srama et al. 2004), is too low to resolve some neighbouring mass peaks. This results in spectra containing broad, joined features comprising peaks from ions with similar masses, such as Na^+, Mg^+, Al^+ and Si^+ or K^+ and Ca^+. To interpret such spectra a manual deconvolution method was applied, similar to the technique that was used to infer compositional information about interstellar dust (ISD) particles (Altobelli et al. 2016). The ISD particles were detected with the same instrument and at similar speeds, affirming the validity of the technique, which was developed further for this study. This method enables spectral ion abundances to be obtained from individual grains by disentangling the neighbouring mass lines.

As a first step, a reference peak was selected, which represents the flight time distribution of a single ion species arriving at the instrument detector. The carbon peak was found to be a suitable candidate, as it is definitely present as a contaminant with an unquantifiable potential contribution from the dust particle in all spectra. For the mass range considered in this work, a Gaussian function was found to be the best approximation to the peak shape. The Gaussian profile was solely fitted using the left (low-mass) flank of the peak, up to the maximum, to avoid the influence of CH^+ ions, which might be present in the right flank and artificially broaden the reference peak. The Gaussian function/reference peak is characterized by three parameters: amplitude, centre (position on the x-axis) and $\sigma^\diamond$ (= FWHM/2.355, where FWHM is the full width at half-maximum of the peak).

The amplitude and position are adjusted individually in each spectrum, to fit the respective ion species into the peak clusters. As higher mass peaks from Na^+ until Ca^+ are slightly broader than the reference C^+ peak in the mass spectra, on average by a factor of 1.1 on the time-of-flight axis, $\sigma^\diamond$ was corrected by a factor of 1.1.

In the Na^+–Si^+ unresolved feature, species' Gaussian shaped peaks were fitted in order of decreasing mass (Fig. S1). Isotopes, such as from Mg, were fitted as individual peaks. First, the reference peak was adjusted in amplitude and position until it matched the right flank of the feature (= Si^+). After a successful fit, this Si^+ fraction was subtracted from the spectrum, leaving a feature with Na^+, Mg^+ and Al^+ ions. Al^+ was skipped, due to the uncertain position between Mg^+ and Si^+. Continuing to move to lower masses, the isotopes of Mg^+, with abundances of about 13 per cent (^{25}Mg) and 14 per cent (^{26}Mg) of the main ^{24}Mg isotope, were fitted next. After all Mg isotopes were subtracted from the spectrum, Na^+ was then fitted on the left flank of the feature. Any residuals between Mg^+ and Si^+ were considered to be Al^+ ions at 27 u. The uncertainty of the 27 u mass line is addressed in Section 3.1. The K^+–Ca^+ feature was treated in the same way as described above, starting with Ca^+.

After all elements were fitted, their spectral abundances could be initially estimated from the Gaussian peak amplitudes. However, iron cation peaks, especially in spectra with high ion yields due to high impact velocity, are often asymmetric and are characterized by an extended left flank. The same effect is visible for the Rh^+ mass lines (Hillier et al. 2006), with left flank shapes dictated by ion energetics and the instrument field geometry. As the left flank of the Fe^+ peak has no signs of obvious contributions from other cations, no

Table 3. List of RSFs (Fiege et al. 2014) used to determine elemental abundances in the silicate particles. Note that the errors are valid for the determination of absolute element abundances in mineral grains but can be neglected if element abundances of two CDA data sets are compared, which is done to compare Fe concentrations in the main text (e.g. Fig. 5). The error of Si is included in the error of the other elements.

Element	Mg	Al	Si	Ca	Fe
RSF (LAMA)	5.5^{+4}_{-2}	3.99^{+3}_{-2}	1	14.12^{+11}_{-6}	$1.32^{+1}_{-0.5}$

deconvolution was performed, and directly measured peak integrals were used. For the few silicate spectra without an Fe^+ peak, an upper limit for the Fe content was estimated from background level and spectral noise in the typical range of the Fe^+ mass line between 53 and 59 u. The integrals of strongly asymmetric Fe^+ peaks were corrected by a factor of 0.9 to accommodate the influence of elements such as Cr, Mn, and Ni in the covered mass range, assuming CI chondritic abundances of these elements relative to Fe.

By applying the deconvolution technique to the data set, the elemental composition of 85 per cent of the individually investigated silicate spectra ('silicate sure', Table 2) could be determined. The remaining 15 per cent either had excessive residuals and/or proved impossible to obtain a suitable reference peak fit.

To compare the peak amplitudes inferred from the fit/manual deconvolution procedure of the Na^+–Si^+ and K^+–Ca^+ features with the integrated Fe^+ abundances, the Gaussian peak amplitudes were converted into peak integrals:

$$\int_{-3\sigma}^{+3\sigma} f(x)\,\mathrm{d}x = \sqrt{2\pi} \times a \times \sigma^{\diamond} \times 1.1 \times \mathrm{erf}\frac{3}{\sqrt{2}}, \quad (2)$$

where a = peak amplitude and $\mathrm{erf}\frac{3}{\sqrt{2}} = 0.9973$.

Na^+ and K^+ abundances are determined in the spectra, but as described above, most likely include or are contamination sources and thus will not be quantified as actual constituents of the particles.

2.5 Relative sensitivity factors

Ionization efficiencies are element-specific, so after extracting the spectral cation abundances, these values were converted to elemental abundances in the particles. This was achieved by applying relative sensitivity factors (RSFs; Table 3, Fiege et al. 2014). These RSFs were determined for orthopyroxene dust grains impacting at velocities between 19 and 25 km s^{-1}, using an electrostatic dust accelerator (Mocker et al. 2011) and an impact ionization mass spectrometer LAMA (Large Area Mass Analyzer; Fiege et al. 2014). They are valid for particle impact speeds from 19 until at least 38 km s^{-1} (Fiege et al. 2014), which covers the range of impact speeds during the Grand Finale orbits. The same RSFs were used in Altobelli et al. (2016) to determine the elemental abundances in ISD particles and, despite the large errors, plausible results were achieved. Hillier et al. (2018) determined RSFs for olivine and although the errors are also large, the derived values lie within the error bars of Fiege et al. (2014).

2.6 Statistical analysis

All details of the statistical evaluation of the data presented in the following Results section are provided in the legends of the respective figures.

Table 4. Mean relative differences of the determined ion abundances inferred with the two deconvolution methods and their standard deviations. Although the mean values of Fe agree very well, the standard deviation is fairly large because of relatively strong scattering of the individual values.

Ion species	Mg	27 u (Al)	Si	Ca	Fe
Mean relative difference	0.08	0.10	0.16	0.25	–0.01
Standard deviation	0.23	0.22	0.30	0.31	0.38

To assess any associated uncertainties with the applied deconvolution technique, the determined ion abundances are compared with the results of an independently developed automated deconvolution algorithm, applied to the same silicate data set, also using the factor of 1.1 to account for changes in peak width with mass. From the peak integrals of the respective ions inferred from individual spectra with the two methods, the relative differences were calculated using

$$\text{Relative difference} = \frac{\mathrm{Int}_{\mathrm{manual}} - \mathrm{Int}_{\mathrm{algorithm}}}{\mathrm{Int}_{\mathrm{manual}}}, \quad (3)$$

where Int_{manual} is the peak integral inferred with the deconvolution technique described in Section 2.4 (equation 2) and $\mathrm{Int}_{\mathrm{algorithm}}$ represents the result of the automated algorithm.

The values of the mean relative differences are given in Table 4. We find that the determined values seem to be element-specific, implying systematic differences in the peak fitting process. The mean relative differences are minor to moderate, with Ca the least in agreement between the two techniques. The manual method delivers, on average, slightly higher abundances for all quantifiable ion species, except for Fe. The standard deviation of the relative differences, however, shows that this trend is likely to not be significant.

3 RESULTS

3.1 Composition

Here, we present the compositional evaluation of the main ring mineral dust particles as seen by Cassini's CDA during the Grand Finale orbits. We find that all spectra with S/Ns sufficient for an individual compositional analysis are dominated by Mg^+ ions, with a smaller Si^+ feature, revealing their siliceous nature. We do not find any spectra indicative of other mineral types like oxides or sulfides in the data set. In general, no Fe-dominated spectra were identified, which are known from CDA analyses elsewhere in the Saturnian system (Fischer et al. 2018; Trieloff et al. 2023).

The elemental ratios of individually analysed silicate spectra ('silicate sure') inferred using a deconvolution technique (see Section 2.4) are shown in Fig. 4. Ion ratios as determined in the spectra before application of relative sensitivity factors (RSFs; Table 3, Fiege et al. 2014) can be found in Fig. 5. The weaker spectra ('silicate weak') of the data set were investigated as one combined co-added spectrum, which increased the S/N to a sufficient level and allowed the average composition of this spectrum class to be quantified.

In addition to the derived silicate particle values, Fig. 4 also shows the expected ratios for CDA ISD particles (Altobelli et al. 2016) and CDA interplanetary dust particles (IDPs; Fischer et al. 2018), both detected by CDA in the Saturnian system with comparable impact speeds on to the instrument. Additionally, the figure shows as reference material bulk values of CI, CH, and LL chondritic material (Lodders & Fegley 1998) and selected cosmochemically

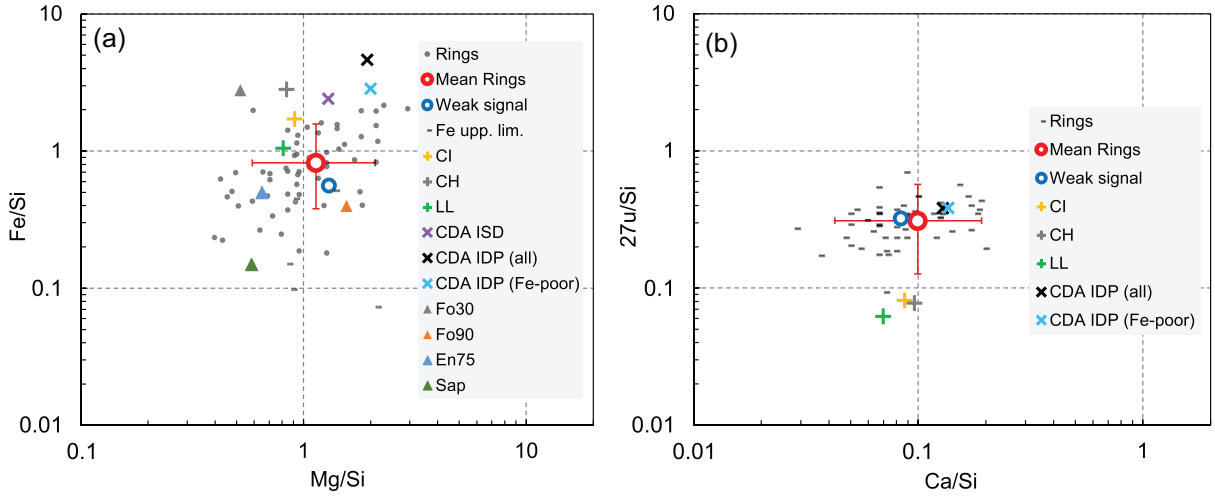

Figure 4. (a,b) Elemental ratios (weight per cent) inferred from spectra of the main ring silicate particles detected during Cassini's Grand Finale orbits. 'Rings' indicates the ratios for individual main ring silicate particles after deconvolution and RSF correction (see Sections 2.4 and 2.5). 'Fe upp. lim.' points represent spectra which do not show a significant Fe^+ mass line, and for which an upper limit was estimated (see Section 2.4). Spectra with S/Ns too low for individual analysis were evaluated combined in a co-added spectrum and the average is displayed as a single data point ('Weak signal'). In addition to IDP and ISD values, where RSFs have also been applied, the element ratios of different chondrites (CI, CH, and LL) are shown. (A) also displays the expected element ratios for Fe-rich ('Fo30') and Fe-poor ('Fo90') olivine, covering significant variation in Mg/Si and Fe/Si, enstatite ('En75') and saponite ('Sap'). The error bars on the mean values are a combination of the doubled standard error of the mean (SEM) and the errors of the RSFs (see Section 2.5).

relevant minerals olivine, enstatite and saponite. Note that at the analysed particle sizes, grain compositions are expected to tend to monomineralicity, and not bulk chondritic compositions.

The majority of the individual data points in Fig. 4 scatter over one order of magnitude, but considering the error bars of the mean ring silicate values (red circles), which represent the standard error of the mean (SEM) combined with the errors of the RSFs (see Table 3), the similarity of Mg/Si and Ca/Si to cosmic (CI chondritic) abundances is significant. The error bars were determined with an error propagation, using the doubled standard error of the mean (2σ significance) of the derived ion ratios and the errors of the RSFs (Table 3). Note that the errors of the RSFs are irrelevant, when directly comparing ion abundances of different spectra, especially when they were recorded with almost identical impact velocities (see Figs 5 and 6).

The main finding is that Fe is significantly depleted with respect to all other references, only LL chondrites still lie within the error bars (Fig. 4a). The Fe/Si ratios of nearly all individual silicate particles are below cosmic (CI chondritic) abundances, on average by a factor of 2.1. Compared with the total averaged IDP population observed in the Saturnian system by CDA, the Fe depletions in the ring silicates are larger, here by a factor of 5. Even the Fe-poor IDP subtype seen by CDA is still less depleted in Fe than the most Fe-rich main ring dust grain of this study. The 'weak signal' spectra show an even smaller Fe/Si ratio compared to 'Mean Rings', indicating a systematic Fe depletion in smaller particles. These observations raise questions related to the mineralogy or potential alteration of the particles, and the subsequent consequences for the pollution of the main rings with interplanetary material (see Section 4).

Another striking observation is that, compared to cosmic abundances, 27 u in the data set is strongly enriched if assumed to be entirely due to Al^+ (Fig. 4b), on average by more than a factor of 3, which could argue for the presence of Al-bearing minerals such as feldspar in the grains. However, we consider the values presented in the figure as an upper limit for Al^+, as a contribution by hydrocarbons seems likely. At these high impact speeds, single C-species are the expected main organic fragments from any kind of hydrocarbon-rich material, including complex compounds, that show up in spectra, followed by C_2 species in proportional amounts (e.g. Hillier et al. 2014). The higher the impact speed or energy density, the stronger the degree of dehydrogenation (Srama 2009; Sephton, Waite & Brockwell 2018). Therefore, $C_2H_3^+$ is expected to be the most abundant C_2 cation and interferes with Al^+ at 27 u making it impossible to distinguish these two ion species. Because of this uncertainty, the peak is called '27 u'. The increased abundance of 27 u implies either a small organic fraction within the particles or a contamination of the CDA CAT, exactly which is yet to be determined. Other species such as $C_2H_4^+$ and $C_2H_5^+$ interfering with Si^+ may be expected as well, though in smaller amounts. Since the determined Si abundances, however, agree roughly with cosmic abundances (Lodders & Fegley 1998), a significant organic interference with Si is considered unlikely. Additionally, we do not identify any spectra with mass lines of N^+, which argues against the presence of HCN^+ ions at 27 u.

Assuming that the ring silicates originate from interplanetary space, they should have compositions similar to those of exogenous particles, if no compositional differentiation or alteration processes are at work. During Cassini's 13 yr in the Saturnian system, CDA produced a comprehensive data set of mineral dust, both in Saturn-bound orbits and of exogenous material. The co-added spectra of the non-icy main ring debris, compared with the exogenous events (Fe-rich and Fe-poor) detected by CDA at similar impact speeds to the sample of this study, excluding the ISD particles identified by Altobelli et al. (2016), are shown in Fig. 5.

3.2 Variation in data

The individual data points (Fig. 4) show a scatter, which reflects the true compositional variations among the particles plus a potential stochastic variation introduced by the impact ionization process. To set the magnitude of the scatter into context, it is compared with the compositional variation of 36 ISD particles detected by CDA in the

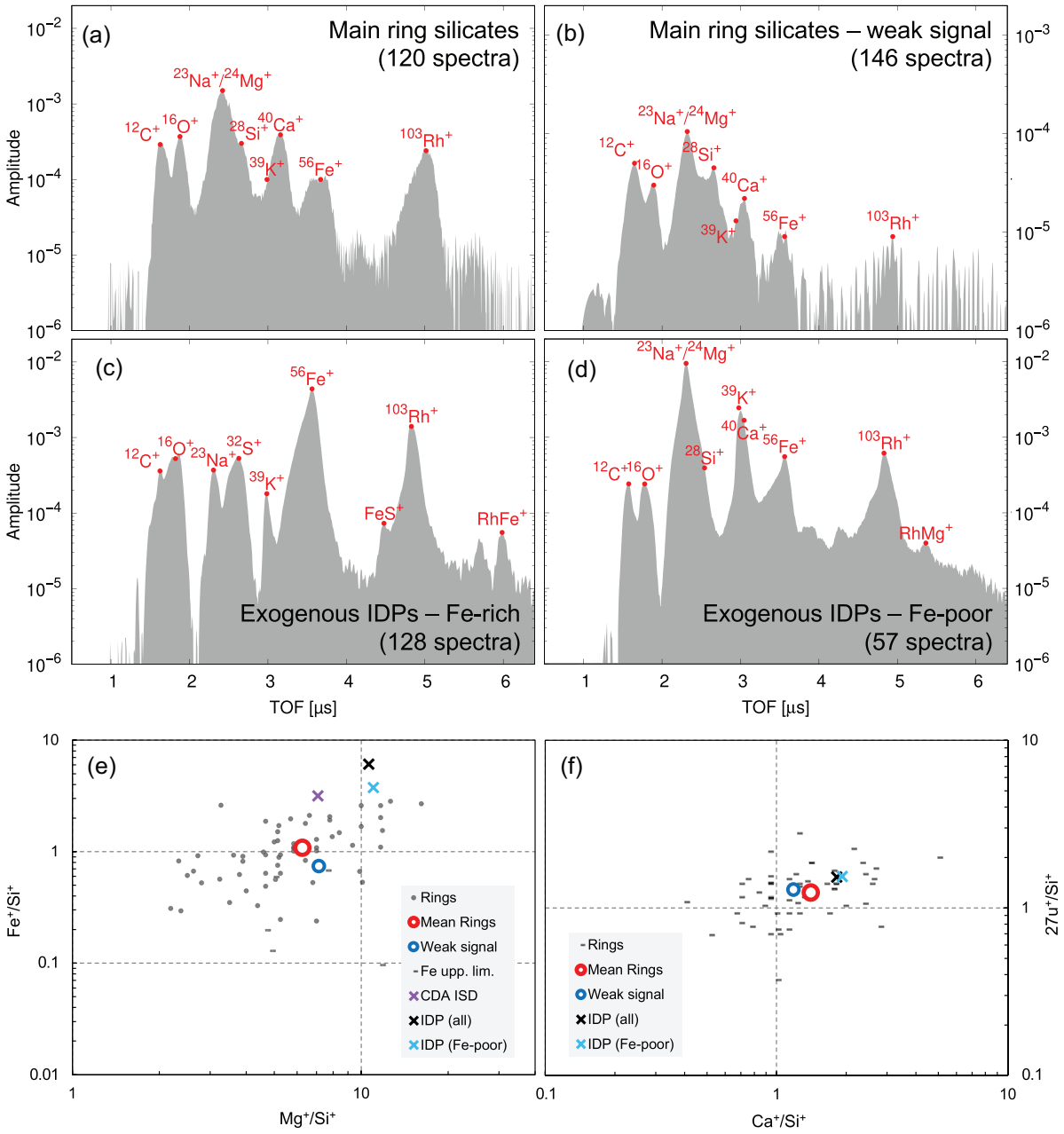

Figure 5. (a–d) Co-added spectra of main ring silicates and the non-icy exogenous IDP populations for comparison. (a) Silicate spectra of the main ring debris with high S/N, (b) 'Weak signal' subset of the main ring silicates, (c) Fe-rich (mostly Fe-sulfides) subset of the exogenous non-icy population recorded in the Saturnian system with similar impact speeds as the main ring debris, and (d) Fe-poor silicate subset of the exogenous population. Note that the *y*-axes in panel (b) covers only three orders of magnitude, while those of the other panels cover four. (e–f) Ion abundance ratios inferred from the spectra of the main ring silicate particles. 'Rings' indicates the ratios for individual particles after deconvolution. We compare these with ion abundances of other compositional families of mineral grains detected by CDA at similar impact velocities. Therefore, the large error introduced by the RSFs (Table 3) – needed to convert ion abundances to element abundances – does not apply here. The error of the depicted mean values is in the order of the symbol sizes. We do not show the error bars for individual detections (Table 4) to avoid an overcrowded plot.

Saturnian system (Altobelli et al. 2016). The result is shown in Fig. 6. Except for a small fraction of the main ring silicates, the degree of compositional variation within each group is similar, and therefore the main ring silicates are considered to be nearly as homogenous as the ISD grains. The Mg/Si ratios are comparable in both data sets. However, the range of variation in the Fe/Ca ratio for the ISD particles is lower, implying that the main ring silicates are less homogeneous in their Fe and/or Ca content. The mean Fe/Ca ratio for the main ring silicates is shifted lower by a factor of 2.2 on average due to the previously mentioned Fe depletion.

3.3 Compositional variation depending on particle size

Figs 4 and 5 indicate a systematic depletion in Fe in the smallest particles ('Weak signal') compared to the average of the remaining

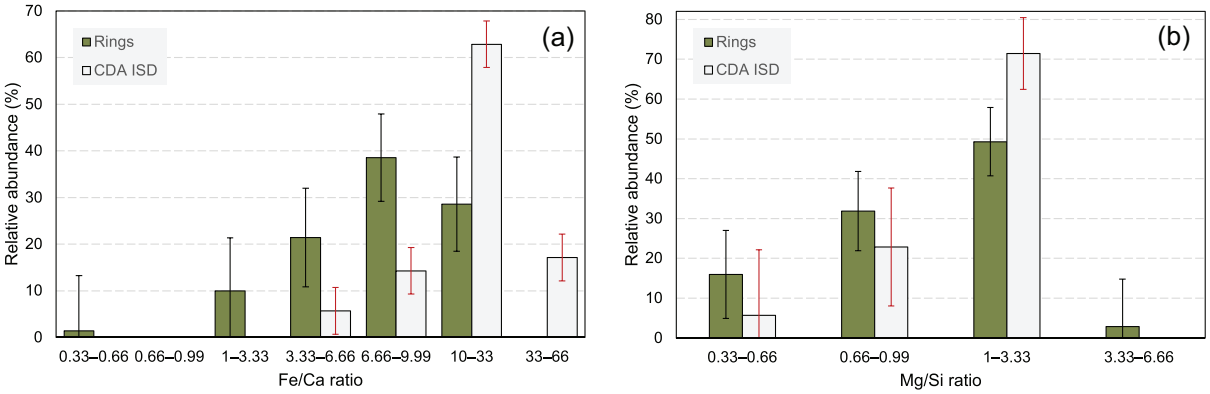

Figure 6. Histograms showing the compositional variation in the main ring silicate data set ('Rings') for the (a) Fe/Ca and (b) Mg/Si ratios. For comparison the variation of ISD particles ('CDA ISD') from a previous CDA analysis (Altobelli et al. 2016) is given. The error bars are defined as $\pm$ sqrt($N \times p \times (1-p)$)/$N \times 100$, with N being the total number of detections per bin, and p the relative abundance defined as probability between 0 and 1.

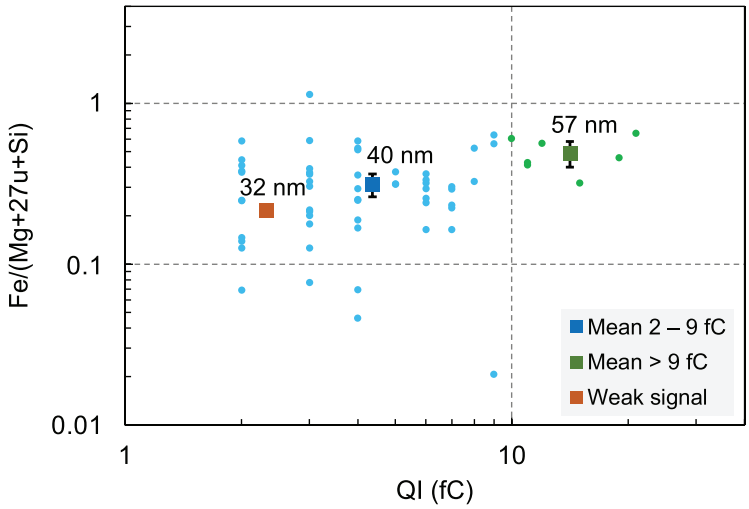

Figure 7. Variation in relative Fe abundances, depending on ion yield QI. For the given similar impact speeds, the QI signals (in fC) are a reasonable approximation for size albeit with large uncertainties (uncertainty of the absolute value is a factor of 2, see Section 2.3). Three size regimes are averaged (2–9 fC, >9 fC and the weak silicate signals with an average value of 2.3 fC) and the values inferred from the respective individual spectra are displayed as blue and green dots. The error bars of the mean values represent the doubled SEM, $\pm$0.05 and $\pm$ 0.09, respectively. The weak signal data point does not show an error since the value was inferred from a single co-added spectrum. Additionally, the approximate equivalent particle radii for the different size regimes are given, calculated from the average QI values and assuming a density of 3 g cm^{-3} (see Section 2.3).

data set ('Mean Rings'). In the following, we investigate this case in more detail.

For any given speed, the ion yield (inferred from the QI signal, which represents the charge arriving at the central ion grid of the CDA) is proportional to the particle mass and depends on the grain composition (see Section 2.3). In Fig. 7, the normalized iron contents of three size regimes are considered to show that the compositional variation depends on particle size. The bigger particles (QI > 9 fC) seem to contain slightly more iron than smaller ones on average. The relatively iron-poor population found in the smaller grains (2–9 fC) with Fe/(Mg + 27u + Si) < 0.3 is absent in the bigger size regime. The Fe abundances of the 'weak signals', representing the smallest observed size regime in this scenario with 2.3 fC on average, are below the other mean values and therefore support this finding. The scatter of data points between 2 and 9 fC is strong, therefore the significance of the difference to the larger size regime is poor. However, the difference between the largest (> 9 fC) and the smallest grains, which show a depletion by a factor of 2.3, is significant: Not one of the seven grains with QI > 9 fC shows iron abundances as low as the weak signal. The average of the data with 2–9 fC confirms this trend and therefore we consider the observed trend noteworthy here.

3.4 Modelling of grain dynamics

In addition to the compositional analysis of the silicate particles, we also investigate their origins. Fig. 1 shows the modelled flux profile and source regions for 20 nm icy grains originating from the main rings and detected by CDA during the Grand Finale orbits (Hsu et al. 2018). This model was refined for this work, focusing on the silicate fraction (Fig. 8), i.e. by assuming a particle density of 3 g cm^{-3}. According to the most frequent particle sizes in the data set (see Fig. 3), we consider spherical particles with three different radii that should correspond (according to the modelling) to different dynamical regimes: 15, 30, and 40 nm. The dynamics of 15 nm particles and smaller are dominated by interaction with

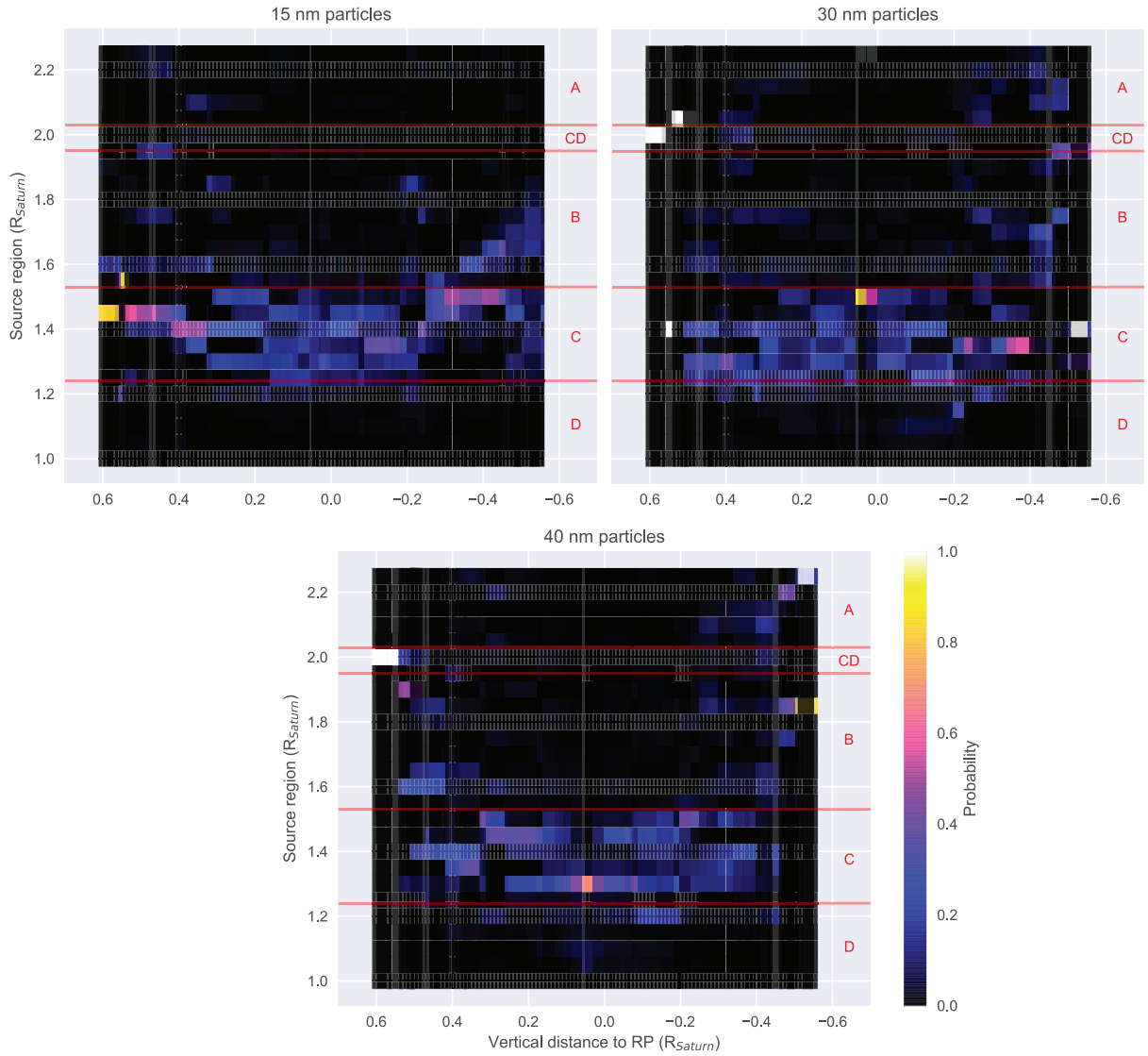

Figure 8. Modelled source regions of silicate particles for three different particle sizes. The *x*-axes show the vertical distance to the ring plane during detection by CDA and the *y*-axes show the radial distance in the equatorial plane of the source region within the main rings. The boundaries of the main ring components are shown in red and labelled on the right. The origin probabilities, normalized to be between 0 and 1, are shown in the key.

Saturn's magnetic field. This grain size roughly represents CDA's lower detection limit. In contrast, the dynamics of particles with radii of 40 nm and above – the larger population of this study – are dominated by their ejection velocities and gravitational forces, with trajectories that become more and more ballistic with increasing size. A radius of 30 nm represents an intermediate case coinciding with a size regime where probably most of the silicate particles detected here lie.

For the simulation, test particles are launched from the main rings, with a distribution weighted according to their surface areas and local optical depths (Hsu et al. 2018). From all the trajectory simulations, the distribution of potential source regions at a given detection location by CDA along the spacecraft trajectory is calculated. For that, the rings are divided into 26 segments, each having a radial extent of $0.05R_S$. For each particle and ring segment, the model provides origin probabilities (normalized to values between 0 and 1) that can be summed up accordingly to derive probabilities for individual particles to originate from a specific ring or, as shown in Table 5, from the inner (C and D rings) or outer ring region (B and A rings). Note, that we restrict the source of the particles to the main rings only. Thus, a potential exogenous origin cannot be further constrained. The particle production mechanism is assumed

Table 5. Silicate particle ratios for origins in the inner (C and D rings) versus outer (B and A rings) main rings. The number of detected dust grains that fulfil the respective probability thresholds (50, 70, and 90 per cent) are given in brackets.

	Ratio inner/outer main ring origin		
Particle radius	15 nm	30 nm	40 nm
Probability > 50 per cent	12 (273)	8 (233)	11.5 (239)
Probability > 70 per cent	51 (208)	8.2 (203)	13.5 (203)
Probability > 90 per cent	50.5 (103)	3.1 (70)	8.6 (125)

to be micrometeoroid impact ejection, hence the production rate is expected to be proportional to the rings' local optical depth, the segment surface areas and the gravitational focusing effect (e.g. Cuzzi & Estrada 1998). As the C ring is known to be more silicate-rich than all other ring segments by about a factor of 5 (Zhang et al. 2017b) we assume a silicate particle production for the C ring five times higher than for the remaining rings. Note that since the silicates are (mostly) embedded in the cores of ring particles, this might make our approach an overestimate, unless much of the material is being ground down in the innermost C ring and being exposed.

The model results imply, independent from the size, that the particles preferably originate from the C ring. For 15 nm grains, the C ring appears to be the clearly dominating source, whereas with larger radii of 40 nm and even more pronounced at intermediate radii of 30 nm, the influence of the outer B and A rings becomes more noticeable (Table 5). Note that even without the applied factor of 5, the contribution from the C ring would be the largest.

We also note that model uncertainties, based on those in the input parameters such as the initial speed distribution (Hsu et al. 2018) and the plasma environment, are present, especially when considering individual grain detections. However, collectively, our results should represent the overall behaviour of ring silicate grains, including identifying their source region(s) as shown in Fig. 8. As stated above, the dynamics of particles with radii of 40 nm and larger are dominated by their ejection velocities. Thus, the ejection velocity is a crucial factor for determining the latitudes bigger particles can reach.

4 DISCUSSION

The infall of exogenous material is generally seen as the most important process driving the compositional evolution of Saturn's main rings. Moreover, through so-called ballistic transport, the rings redistribute their angular momentum via the transport of ejecta produced by micrometeoroid bombardment. For instance, this process has been shown to explain the optical depth structure across the B and C ring boundary (Ip 1983; Cuzzi & Estrada 1998; Estrada et al. 2015). A widely accepted assumption is that Saturn's rings consisted of pure water ice when they formed. The non-icy components gradually 'colour' the rings, in accordance with the aforementioned dynamical effects, and are assumed to originate from exogeneous material (IDPs and ISD), which polluted the rings over time (Cuzzi & Estrada 1998; Cuzzi et al. 2009; Zhang et al. 2017a, b; Estrada & Durisen 2023). A potential exception is the C ring, the composition of which might have been significantly affected by the more recent break-up of a large object (Zhang et al. 2017b). The actual colouration of the rings depends on the ratio between the infalling and outgoing silicate flux. This is the basis by which the age of Saturn's rings was calculated recently, using the amount of polluting material found by Cassini instruments in the rings, the ring mass determined by Cassini, and the IDP flux inferred from measurements by CDA's Entrance Grid (EG) subsystem (Kempf et al. 2023). Note that the EG subsystem is only sensitive to large grains (radii larger than $\sim$1.5 µm; Kempf et al. 2023), which tend to be massive enough to produce impact charge yields which saturate CDA's Chemical Analyzer (CA) subsystem. Thus, they do not produce interpretable spectra, and direct compositional measurements of the large polluting IDPs have not been obtained.

No significant organic-rich dust population has currently been identified in the low-mass end of the exogenous material accessible for compositional analysis (Fischer et al. 2018), although the larger IDPs analysed in Kempf et al. (2023) are assumed to have a significant fraction of organics. We also see no purely organic dust population leaving the rings into Saturn in the spectra investigated here. However, the overabundance of ions with mass 27 u in the silicate spectra (see Section 3) can potentially be explained by small contributions of organic material ($C_2H_3^+$) that could be fragments from larger hydrocarbons, but it is currently unclear if this material can be attributed to the particles or a contamination of the CDA's impact target. However, even if we consider the 27 u excess being entirely due to organics, CDA still finds clearly less organic material falling into Saturn than Cassini's Ion and Neutral Mass Spectrometer (INMS) in extremely small grains ($\sim$1 nm, e.g. Waite et al. 2018; Miller et al. 2020) and as Kempf et al. (2023) assume (30 per cent organics) for more massive IDPs hitting the rings.

We find that the compositions of the material potentially contaminating the mostly icy rings of Saturn and of the non-icy material emitted by the rings that eventually falls into Saturn are very different. The factor of 5–6 depletion of Fe (shown by the Fe/Si ratio) compared to the exogenous IDP particles (Fig. 4a) is striking. The drastic differences in the average Fe abundance are predominately caused by a very Fe-rich IDP subpopulation, mostly made of Fe-sulfides (Fig. 5c), which is entirely missing in the ring debris data set of this work. Since the measurements of both non-icy populations were made with the same instrument, they are directly comparable and an instrument artefact leading to the observed differences can be ruled out. There is also a noticeable difference in the compositional diversity: while the minerals measured in the identified main ring particles only show a moderate scatter in their Mg, Ca, and Fe abundances, exclusively consisting of Mg-rich/Fe-poor silicates, the exogenous IDPs observed by CDA in the Saturnian system clearly possess a variety of different mineral types, such as silicates, sulfides and oxides (Fischer et al. 2018). However, even the relatively Fe-poor silicate subset of the exogenous material (Fig. 5d) shows a higher Fe/Si ratio of 2.8 – comparable to CH chondritic abundances (Fig. 4a) – than the main ring silicates.

Within the compositionally homogenous silicate component of main ring debris we find no indication for large compositional variations reaching Saturn from different regions of the rings. The only compositional trend that we found is a weakly significant systematic decrease in Fe in smaller particles (Fig. 7).

Thus, CDA measurements show the composition of dust lost by the rings into Saturn is distinctly different from that of the IDPs bombarding the rings, assuming that the smaller IDPs accessible for compositional analysis are part of the same population as the larger grains discussed in Kempf et al. (2023). One main result of this work therefore is that we find no indication of Saturn being a major sink for pristine contemporary IDPs falling on to Saturn's rings. This becomes even more remarkable if we consider that the flux of silicates falling into Saturn could potentially amount to a significant fraction of the flux of silicates falling on to the rings (Hsu et al. 2018; Kempf et al. 2023).

In the following, we will discuss several possible explanations for these observations, noting that more than one of these scenarios might be applicable simultaneously.

(1) Observational bias, infalling IDPs: The composition of contemporary IDPs measured by CDA is not representative of the bulk IDP composition responsible for ring contamination.

(2) Observational bias, outgoing nanodust: The material currently falling in from the rings towards Saturn is not representative of the bulk composition of the rings.

(3) Ring silicates falling into Saturn originate mostly from IDPs but have been compositionally modified (i.e. depleted in Fe) by physical and/or chemical processes within the rings.

(4) IDPs are not responsible for the greater part of the silicates found in the rings and there is a more dominant source for siliceous material (e.g. from a disrupted large object which formed the rings in the first place).

Scenario (1) is the case in which the exogeneous dust detected by CDA is compositionally different from the IDPs that have contaminated the main rings in the past. This could either be due to a change in IDP composition over time (Scenario 1a), or due to a selection effect in the IDPs that were sampled by CDA between 2004 and 2016 (Scenario 1b).

(i) 1a: We consider the first reason to be unlikely, since what is currently known about the evolution of the Solar system regarding the most relevant IDP source bodies in the Kuiper belt (Kempf et al. 2023), suggests a fairly stable bulk dust composition falling onto the rings over a time span of 100–200 My [the current estimated age of the main rings (Estrada & Durisen 2023; Kempf et al. 2023)].

(ii) 1b: An observational bias in the IDP sample accessible for compositional analysis by CDA is possible. As mentioned above, the CA subsystem is insensitive to grains that are too large, and generate an overabundance of ions upon impact. Although this is not relevant for the Grand Finale ring debris sample of this study (see Fig. 3), it limits the CDA IDP compositional survey in the Saturnian system to dust radii of about 0.5 μm or smaller. The mass flux, however, is generally assumed to be dominated by larger grains with radii above 50 μm and although these particles have indeed been measured by CDA's EG subsystem of CDA (Kempf et al. 2023), they are inaccessible for compositional analysis. Therefore, if the composition of the larger IDPs dominating the mass flux is different to that of the submicron-sized grains as seen by CDA (Fig. 5, Fischer et al. 2018), this could explain the observations.

Scenario (2) assumes that the ring debris falling into Saturn stems from an atypical ring region (Scenario 2a), is caused by a transient event (Scenario 2b), or is prone to a dynamical selection effect (Scenario 2c) and thus is not representative of the ring bulk silicates:

(i) 2a: Remote sensing by Cassini has shown that the C ring, although much less massive than the B and A rings, bears the largest fraction of non-icy material in Saturn's ring system. This anomaly has been attributed to disruption of a large body—probably a Centaur—introducing additional siliceous material into the C ring and roughly doubling the ring's mass (Zhang et al. 2017a, b). Although the high silicate-to-ice particle detection ratio of 33 per cent (Hsu et al. 2018) measured during the Grand Finale orbits does not agree with the silicate volume abundances measured in any of the main rings via remote sensing, namely $<$ 1 per cent for the A and B rings, rising to 4–9 per cent for the C ring (Zhang et al. 2017a, b), it is still in better agreement with a C ring origin and comes close to the silicate mass fraction of 14–32 per cent there (using the volume fraction above, a density of 3 g cm^{-3} for silicates, and 0.92 g cm^{-3} for water ice). Hence, the silicate population measured by CDA should be dominated by C ring silicates, mostly made of silicates from a hypothetically Fe-depleted disrupted body, unlike the presumably exogenous, Fe-rich grain dominated material in the B ring. As shown in Fig. 8, the material detected during the Grand Finale orbits – although mainly originating from the C ring – occasionally also probes the A and B rings. However, the spectra produced by grains that with high probability stem from these outer rings do not show any noticeable compositional difference to those from the C ring (Fig. S2) and thus we have no indication for a compositionally distinct population of silicates originating from the C ring. In fact, Fig. 4 shows that there is not a single measured rocky dust grain falling into Saturn that comes even close to the average Fe abundance CDA finds in IDPs.

(ii) 2b: A recent violent event has been suggested to explain other Cassini measurements during the Grand Finale (e.g. Perry et al. 2018; Waite et al. 2018; Serigano et al. 2022; Moses et al. 2023). Similarly, such an event could potentially serve as a transient source of the observed Fe-depleted silicates. However, the corresponding effects of such an event are expected to be limited to the inner D ring region near the ring plane (e.g. Perry et al. 2018), contrasting with the fact that ring silicates have been measured up to 0.5R_S away from the ring plane (Fig. 1), which are not reachable for D ring debris. This suggests a dynamical connection of the ring silicates to the entire main rings instead of a transient event at the inner D ring or a localized source in the rings. In addition, there is no clear compositional connection between Fe-depleted silicates observed by CDA and the organic-rich compounds seen by Cassini's INMS that were reported to originate from such an event (Waite et al. 2018), but are largely missing in the CDA data set investigated here. In summary, our results do not support this scenario.

(iii) 2c: A mechanism that preferentially delivers Fe-poor silicates into Saturn, while Fe-rich phases preferentially remain in the rings, would explain our observation. The significantly enhanced silicate-to-ice ratio of these ring debris (Hsu et al. 2018) compared to the bulk composition of the rings could already hint at such a selective process (Zhang et al. 2017a, b; Crida et al. 2019). Such a selective dynamical process could be due to chemical or physical (mass, charge, density) parameters. Indeed, from our data set it is striking that, from over 1000 dust detections (see Section 2.1), none created an impact charge larger than 230 fC (equivalent to a particle radius of about 120 nm), despite the CA subsystem of CDA being sensitive to particles up to about 10 times more massive. If we assume that electromagnetic interaction is the dominant effect delivering charged dust particles into Saturn (Hsu et al. 2018), this automatically limits the mass and size. Larger particles, the dynamics of which are not dominated by electromagnetic forces, would need very high ejection velocities after micrometeoroid impact to ballistically fall into Saturn, which eventually becomes a limiting factor. However, it is currently unclear how such a mass-selective effect could be linked to chemical fractionation (i.e. why Fe-rich phases common in the ring material should be depleted in the dust grains with radii below $\sim$100 nm falling into Saturn). Maybe the higher densities of Fe-rich phases (see Scenario 3) could be a physical discriminator for chemical fractionation of Saturnian dust infall.

Scenario (3): The CDA observation that even the IDP population with the lowest Fe abundance is not as depleted in iron as the main ring silicates (Figs 4 and 5) implies that – even if we find a subsequent selective transport process (Scenario 2) – the infalling IDPs need to undergo a chemical alteration within the rings first. To explain the physical (Scenario 3a) or chemical (Scenario 3b) alteration of initially Fe-rich mineral IDP phases, we consider modification when IDPs collide with the main rings and during subsequent ballistic transport by which ring material is repeatedly redistributed within the ring system by impact ejecta processes (Cuzzi & Durisen 1990; Durisen et al. 1992; Cuzzi & Estrada 1998).

(i) 3a: A possible physical process that would work at IDPs impacting on to the main rings with speeds of 10 s of km s^{-1} is the impact ionization of Fe by the kinetic energy of the impact and subsequent removal of these Fe^+ ions into the magnetosphere. Suprathermal Fe^+ ions were measured in Saturn's magnetosphere

and their radial distribution indicates a source located inwards of Enceladus' orbit (Christon et al. 2015). Christon et al. (2015) indeed suggest IDPs partially ionizing when impacting Saturn and the main rings at hypervelocities, as a likely source for the suprathermal Fe^+ population. If Fe escapes more efficiently than other constituents, the remaining recondensed material would be Fe-depleted and could account for the homogeneous Fe-depleted silicates observed in this work. However, since the Fe concentration in infalling IDPs differs by more than a factor of 5 from dust falling into Saturn, it seems questionable whether more than 80 per cent of the infalling Fe (more than 50 kg s^{-1}, using the total flux numbers by Kempf et al. 2023) can be removed in the form of Fe^+ without removing the other IDP constituents by a similar process. The low ionization yield (RSF) for Fe compared to other rock forming elements like Mg or Ca (Fiege et al. 2014) argues against that. Indeed, observations by Christon et al. (2014) report the presence of a large number of ions potentially stemming from other rock forming elements. Ions with masses of ∼28 u – that could at least partially be attributed to Si^+ – exhibit similarly increased abundances in the inner Saturnian system as Fe^+. The data also show a small peak in agreement with Ca^+ (40 u) observed in Saturn's equatorial magnetosphere and a high noise floor at Mg^+ (24 u) in principle allowing the presence of magnesium ions (Christon et al. 2014). Therefore, the data show no hint for a specifically efficient removal of Fe^+ from the main ring or infalling IDP material compared to other rock-forming ions, although we note that Mg^+ is not quantifiable with the same level of significance as the other rock-forming ion species due to signal interference with water-related ions (Christon et al. 2014).

(ii) 3b: We consider that chemical alteration of the original IDP minerals by evaporation and recondensation processes during the initial collisions of IDPs with the rings, as well as during subsequent ballistic transport, is highly likely (e.g. Chernonozhkin et al. 2021; Kempf et al. 2023). Upon impact on to larger, mostly icy, ring material, infalling IDPs will inevitably evaporate at impact speeds of 15 km s^{-1} and above (e.g. Postberg et al. 2014) thereby mixing with water vapor released from the struck icy ring material it has hit. Most of the infalling Fe in such IDPs (that are small enough for CDA to measure the composition of) comes in the form of sulfides (Fig. 5c; Fischer et al. 2018). Due to the oxidizing conditions in a water vapor environment, recondensation as metal or sulfide is effectively prevented in favour of Fe-oxides and SO_2 (e.g. Wozniakiewicz et al. 2011). Similarly, though much less efficiently, IDPs composed of Fe-bearing silicates, that evaporate upon impact and mix with water vapor, could become depleted in Fe in favour of FeO formation as it has been observed by aqueous alteration of GEMS (glass with embedded metal and sulfide) grains (Keller & Snead 2022). Such a process could over time – maybe supported by repeated heating, melting and/or evaporation and condensation during the ballistic transport (Durisen & Estrada 2023) – effectively lead to a conversion of the IDP minerals into two main phases: Fe-rich oxides and Fe-depleted silicates. SO_2 would volatilize over geological time-scales and only traces of sulphur can still be found in a few silicate particles leaving the rings into Saturn (see Fig. 2b). There is a recent finding by *JWST* observations that supports the idea of processing of ring material at elevated temperatures: Hedman et al. (2024) report that ices in Saturn's main rings are strongly dominated by crystalline water ice. At temperatures that – from solar illumination – always stay below 120 K (e.g. Altobelli et al. 2008), substantial amounts of amorphous ice are expected to form from radiation damage over geological time-scales. The entirely crystalline ring ice could therefore be an indicator of the same efficient heating and recondensation processes triggered by IDP impacts and ballistic transport of ring material we propose here.

Scenario (4) would question a fundamental assumption in the generation of Saturn's rings, i.e. that the rings started their existence as an almost pure water ice entity and that the current non-icy material was deposited later via IDPs (e.g. Cuzzi & Estrada 1998). The most credible scenario for the generation of the rings – the disruption of a moon or another large body by tidal forces or collision (Roche 1849; Charnoz et al. 2018; Wisdom et al. 2022; Teodoro et al. 2023) – indeed easily allows the ab initio availability of non-icy material as ring constituents.

(i) 4a: In a scenario like the disruption of a large, differentiated moon, it would be more likely to create a ring with substantial amounts of mantle silicate (e.g. Harris 1984; Dones 1991) than one of almost pure water ice (Charnoz et al. 2018; Wisdom et al. 2022). The Fe-rich IDPs that have impacted the ring since its creation would then only be a minor constituent of a ring silicate composition which is otherwise dominated by mantle material from an early moon. The Fe deficiency (when compared to chondritic or solar abundances) of the ring particles measured by CDA would require the precursor body to be differentiated, with Fe-poor mantle material preferentially surviving in the rings, while the denser, Fe-rich core material fell into Saturn after disruption of the former moon.

(ii) 4b: Another possibility is that the bulk of a smaller – not necessarily differentiated – precursor body was Fe-poor. For example, there are chondritic parent bodies with primordial low abundances of Fe, e.g. the parent bodies of LL chondrites (see Fig. 4 and Abe et al. 2006; Okada et al. 2006). However, such a scenario would imply an old ring age, which would be in disagreement with the age estimates from Kempf et al. (2023), and the body needed to be sufficiently large to create the entire ring. Thus, we consider the differentiated large body from Scenario 4a as more plausible.

Scenario 4 is hard to reconcile with Cassini remote sensing data of the main rings that support a maximum average silicate abundance of less than 1 per cent by volume averaged over the entire ring (Zhang et al. 2017a, b), although improved constraints resolving the ongoing debate about the composition of the non-icy material by a future mission could well change the picture. Using the Cassini upper limit on silicate material, an origin of this silicate fraction in mantle material of a disrupted moon instead of IDPs would imply a substantially lower ring age than the 100–200 My inferred by Kempf et al. (2023) from IDP contamination. Since the overwhelming amount of silicates needs to stem from the Fe-depleted mantle material of the moon, the age of the ring would be less than a few million years, which is younger than any currently discussed scenario (Crida et al. 2019; Wisdom et al. 2022; Estrada & Durisen 2023; Kempf et al. 2023). Additionally, the break-up of such a disrupted large object entraining significant amounts of material into the C ring would not explain the observed anticorrelation of a high non-icy fraction in the C ring and its low optical depth (e.g. Zhang et al. 2017a, b), an effect also observed in the Cassini division.

5 CONCLUSIONS

The composition of Saturn's main rings is of high scientific interest, providing constraints on their vividly debated origin and age (Crida et al. 2019; Ida 2019). One scenario suggests that the mid-sized Saturnian satellites and the ring moons have accreted (Charnoz et al. 2011; Crida & Charnoz 2012; Salmon & Canup 2017) from a formerly more massive and expanding ring (Salmon et al. 2010).

We have analysed the non-icy fraction of dust particles falling into Saturn that have been mobilized by impacts on to Saturn's main rings. This dust population was sampled by Cassini's CDA during the Grand Finale orbits, between the planet and the inner edge of the rings. The high impact speeds ($\sim$30 km s^{-1}) of the dust particles on to the instrument allowed the elemental compositions of particles only 10 s of nm in size to be measured. The compositions were determined from CDA's TOF relatively low-resolution mass spectra by applying a deconvolution technique, revealing a relatively homogenous composition of Mg-rich silicates with Mg, Si, and Ca similar to CI chondritic values; Fe, however, was found to be significantly depleted. The Al abundance could not be reliably quantified because of a potential interference with small amounts of hydrocarbons that are either a minor particle constituent or stem from contamination of CDA's impact target.

We observe no compositional variation between particles depending on their origin from the A, B, or C rings. In comparison with exogenous IDPs encountered by CDA in the Saturnian system, the ring material shows an even starker contrast in Fe abundances. The observed IDPs exhibit a more than 5 times higher Fe abundance, mostly due to an iron-sulfide IDP sub-population, which is entirely missing in the homogenous main ring dust. Even though an overestimation of the IDP Fe abundance by CDA is possible (see below and Scenario 1b), such a stark discrepancy is unexpected since IDPs are thought to be the main supplier of non-icy material on to the otherwise icy rings (e.g. Kempf et al. 2023). Thus, we conclude that Saturn cannot be a major sink for unaltered contemporary IDPs falling onto Saturn's rings.

In Section 4, we have discussed several scenarios for the observed compositional discrepancies between the mineral compositions of IDPs falling on to the rings and those of dust leaving the rings towards Saturn. In the following, we discuss the most likely of the above scenarios and their implications. We conclude that, although there are alternative possibilities, all currently available observations are in agreement with a combination of Scenarios (3b) and (1b) to explain the drastic depletion in Fe that we have found in the nano-sized silicate particles from the rings: chemical alteration of IDPs in the rings (3b) possibly combined with an observational bias in the IDP data set accessible for CDA's compositional analysis (1b). The greater part of the IDP flux entering the Saturnian system originates from the Kuiper belt (Kempf et al. 2023). An observational bias, introduced by CDA's ability to assess only the composition of small, submicron-sized IDPs entering the Saturnian system and falling on to the rings (1b) would become relevant if Fe-rich phases would be preferentially concentrated in submicron-sized grains of the IDP flux, while Fe-poor minerals are systematically 'hidden' from CDA in larger grains (that CDA's Chemical Analyzer cannot observe). Such a scenario is indeed supported by recent findings that the infalling Kuiper belt dust might contain an unusually high fraction of Fe-rich phases concentrated in the small sub-µm aggregates (Keller & Snead 2021; Keller & Flynn 2022). However, it is highly uncertain if these findings, from investigations of a small number of potential Kuiper belt dust grains found on Earth (Keller & Snead 2021; Keller & Flynn 2022) are representative of the bulk composition of IDPs from the Kuiper belt entering the Saturnian system. The composition – and even more the compositional fractionation – of such dust is currently poorly constrained.

We think that chemical high temperature alteration of impacting IDPs from Fe-sulfides (and potentially silicates) leading to the formation of Fe-oxides is inevitable (3b). Interestingly, the detection of three Fe-rich grains – in addition to nine Fe-poor silicates – just outside the F ring by CDA during Cassini's Ring-Grazing orbits preceding the Grand Finale is reported by Linti et al. (2024b). Spectral analysis of the Fe-rich grains identifies them as oxides, consistent with hematite. Although these grains could stem from the A or B rings, we note this interpretation is not unique because several other dust sources mix in the region just outside the main rings (Linti et al. 2024b). However, no Fe-oxides (nor Fe-sulfides) are detected in the data set discussed in this work, sampled radially inwards of the main rings. Together with the Fe depletion in the observed silicate dust, this finding implies an accumulation of Fe-rich minerals – mostly Fe-oxides – in the main rings over time. Indeed, the presence of nanophase hematite or metallic iron in the Saturnian system, and particularly in the main rings, is suggested by earlier studies (Clark et al. 2008; Stillman & Olhoeft 2008; Cuzzi et al. 2009) and discussed as an important UV-absorber. Other space weathering mechanisms that produce nanophase iron are also known and could be relevant in further modifying the composition of Saturn's rings (Pieters & Noble 2016). The dynamical reason and the preferred removal of Fe-poor silicates leaving Fe-rich phases behind, currently remains elusive and we are left with mere speculations (see Scenario 2c).

ACKNOWLEDGEMENTS

The research in context of this work was supported by the European Space Agency under the contract 4000118000/16/ES/JD, and the European Research Council Consolidator grant 724908-Habitat OASIS. Jon K. Hillier thanks the Deutsche Forschungsgemeinschaft (DFG) for funding under grant HI-2157/1–1. The authors thank Larry Esposito, Kelly Miller, and the International Space Science Institute (ISSI) for the opportunity of valuable discussions.

DATA AVAILABILITY

All data needed for the analysis are available in the main text or the supplementary materials. The CDA data underlying this article are available on the Small Bodies Node of the Planetary Data System (PDS-SBN), at https://sbn.psi.edu/pds/resource/cocda.html.

REFERENCES

Abe M. et al., 2006, Science, 312, 1334
Altobelli N. et al., 2016, Science, 352, 312
Altobelli N., Spilker L. J., Leyrat C., Pilorz S., 2008, Planet. Space Sci., 56, 134
Bradley E. T., Colwell J. E., Esposito L. W., in review
Charnoz S. et al., 2011, Icarus, 216, 535
Charnoz S., Canup R. M., Crida A., Dones L., 2018, Planetary Ring Systems: Properties, Structure, and Evolution. Cambridge Univ. Press, Cambridge, p. 517
Chernonozhkin S. M. et al., 2021, Nat. Commun., 12, 5646
Christon S. P., Hamilton D. C., Mitchell D. G., DiFabio R. D., Krimigis S. M., 2014, J. Geophys. Res., 119, 5662
Christon S. P., Hamilton D. C., Plane J. M. C., Mitchell D. G., DiFabio R. D., Krimigis S. M., 2015, J. Geophys. Res., 120, 2720
Clark R. N. et al., 2008, Icarus, 193, 372
Clark R. N. et al., 2012, Icarus, 218, 831
Connerney J. E. P., 1986, Geophys. Res. Lett., 13, 773
Crida A., Charnoz S., 2012, Science, 338, 1196
Crida A., Charnoz S., Hsu H.-W., Dones L., 2019, Nat. Astron., 3, 967
Cruikshank D. P., Imanaka H., Dalle Ore C. M., 2005, Adv. Space Res, 36, 178
Cuzzi J. N., Clark R. N., Filacchione G., French R. G., Johnson R., Marouf E., Spilker L., 2009, Saturn from Cassini-Huygens, Springer, Dordrecht, p. 459
Cuzzi J. N., Durisen R. H., 1990, Icarus, 84, 467

Cuzzi J. N., Estrada P. R., 1998, Icarus, 132, 1
Cuzzi J. N., French R. G., Hendrix A. R., Olson D. M., Roush T., Vahidinia S., 2018, Icarus, 309, 363
de Pater I., Dickel J. R., 1991, Icarus, 94, 474
Dones L., 1991, Icarus, 92, 194
Dougherty M. K., Esposito L. W., Krimigis S. M., 2009, Saturn from Cassini-Huygens. Springer, Dordrecht
Durisen R. H., Bode P. W., Cuzzi J. N., Cederbloom S. E., Murphy B. W., 1992, Icarus, 100, 364
Durisen R. H., Estrada P. R., 2023, Icarus, 400, 115221
Estrada P. R., Durisen R. H., 2023, Icarus, 400, 115296
Estrada P. R., Durisen R. H., Cuzzi J. N., Morgan D. A., 2015, Icarus, 252, 415
Fiege K., Trieloff M., Hillier J. K., Guglielmino M., Postberg F., Srama R., Kempf S., Blum J., 2014, Icarus, 241, 336
Fischer C., Postberg F., Altobelli N., Nölle L., Albin T., 2018, EPSC, 12, 1279
Harris A. W., 1984, in Greenberg R., Brahic A., eds., IAU Coll. 75, Planetary Rings. Univ. Arizona Press, Tucson, AZ
Hedman M. M. et al., 2024, JGR Planets, in press
Hillier J. K. et al., 2014, Planet. Space Sci., 97, 9
Hillier J. K., McBride N., Green S. F., Kempf S., Srama R., 2006, Planet. Space Sci., 54, 1007
Hillier J. K., Postberg F., Sestak S., Srama R., Kempf S., Trieloff M., Sternovsky Z., Green S. F., 2012, J. Geophys. Res., 117, E09002
Hillier J. K., Sternovsky Z., Kempf S., Trieloff M., Guglielmino M., Postberg F., Price M. C., 2018, Planet. Space Sci., 156, 96
Hsu H.-W. et al., 2018, Science, 362, eaat3185
Ida S., 2019, Science, 364, 1028
Ip W.-H., 1983, Nature, 302, 599
Keller L. P., Flynn G. J., 2022, Nat. Astron., 6, 731
Keller L. P., Snead C. J., 2021, Goldschmidt 2021.
Keller L. P., Snead C. J., 2022, 85th Annual Meeting of the Meteoritical Society, LPI Contributions, 2695, 6506, Glasgow, Scotland
Kempf S., Altobelli N., Schmidt J., Cuzzi J. N., Estrada P. R., Srama R., 2023, Sci. Adv., 9, eadf8537
Linti S., Khawaja N., Hillier J. K., Nölle L., Fischer C., Hsu H.-W., Srama R., Postberg F., 2024b, MNRAS, stae238
Lodders K., Fegley B., 1998, The planetary scientist's companion, Oxford Univ. Press, New York
Miller K. E. et al., 2020, Icarus, 339, 113595
Mocker A. et al., 2011, Rev. Sci. Instrum., 82, 095111
Morris R. V., Lauer H. V., Jr., Lawson C. A., Gibson E. K., Jr, Nace G. A., Stewart C., 1985, J. Geophys. Res., 90, 3126
Moses J. I. et al., 2023, Icarus, 391, 115328
Nicholson P. D. et al., 2008, Icarus, 193, 182
Northrop T. G., Hill J. R., 1982, J. Geophys. Res., 87, 6045
Okada T., Shirai K., Yamamoto Y., Arai T., Ogawa K., Hosono K., Kato M., 2006, Science, 312, 1338
Perry M. E. et al., 2018, Geophys. Res. Lett., 45, 10,093
Pieters C. M., Noble S. K., 2016, J. Geophys. Res., 121, 1865
Pollack J. B., 1975, Space Sci. Rev., 18, 3
Postberg F. et al., 2014, Meteorit. Planet. Sci., 49, 1666
Postberg F., Kempf S., Rost D., Stephan T., Srama R., Trieloff M., Mocker A., Goerlich M., 2009a, Planet. Space Sci., 57, 1359
Postberg F., Kempf S., Schmidt J., Brilliantov N., Beinsen A., Abel B., Buck U., Srama R., 2009b, Nature, 459, 1098
Postberg F., Schmidt J., Hillier J., Kempf S., Srama R., 2011, Nature, 474, 620
Roche E., 1849, Académie des Sciences et des Lettres de Montpellier, 1, 243
Salmon J., Canup R. M., 2017, ApJ, 836, 109
Salmon J., Charnoz S., Crida A., Brahic A., 2010, Icarus, 209, 771
Sephton M. A., Waite J. H., Jr., Brockwell T. G., 2018, Astrobiology, 18, 843
Serigano J., Hörst S. M., He C., Gautier T., Yelle R. V., Koskinen T. T., Trainer M. G., Radke M. J., 2022, J. Geophys. Res., 127, e2022JE007238
Spilker L., Ferrari C., Cuzzi J. N., Showalter M. R., Pearl J. C., Wallis B., 2003, Planet. Space Sci., 51, 929
Srama R. et al., 2004, Space Sci. Rev., 114, 465
Srama R., 2009, Habilitation thesis, Univ. Stuttgart
Stillman D., Olhoeft G., 2008, J. Geophys. Res., 113, E09005
Teodoro L. F. A., Kegerreis J. A., Estrada P. R., Ćuk M., Eke V. R., Cuzzi J. N., Massey R. J., Sandnes T. D., 2023, ApJ, 955, 137
Trieloff M., Fischer C., Postberg F., Schmidt J., 2023, EGU General Assembly, EGU23-16469, Vienna, Austria
Waite J. H., Jr. et al., 2018, Science, 362, aat2382
Wisdom J., Dbouk R., Militzer B., Hubbard W. B., Nimmo F., Downey B. G., French R. G., 2022, Science, 377, 1285
Wozniakiewicz P. J. et al., 2011, Meteorit. Planet. Sci., 46, 1007
Zhang Z. et al., 2017b, Icarus, 281, 297
Zhang Z., Hayes A. G., Janssen M. A., Nicholson P. D., Cuzzi J. N., de Pater I., Dunn D. E., 2017a, Icarus, 294, 14

SUPPORTING INFORMATION

Supplementary data are available at *MNRAS* online.
Please note: Oxford University Press is not responsible for the content or functionality of any supporting materials supplied by the authors. Any queries (other than missing material) should be directed to the corresponding author for the article.

This paper has been typeset from a TEX/LATEX file prepared by the author.